

# Radiation damage reveals promising interaction position

Cornelia Koch, Andreas Heine and Gerhard Klebe\*

Received 10 September 2010

Accepted 12 July 2011

Philipps-Universität, Marburg, Germany. E-mail: klebe@mail.uni-marburg.de

PDB References: 3onc; 3onb.

High-resolution structural data of protein inhibitor complexes are the key to rational drug design. Synchrotron radiation allows for atomic resolutions but is frequently accompanied by radiation damage to protein complexes. In this study a human aldose reductase mutant complexed with a bromine-substituted inhibitor was determined to atomic resolution [Protein Data Bank (PDB) code 3onc]. Though the radiation dose was moderate, a selective disruption of a bromine–inhibitor bond during the experiment was observed while the protein appears unaffected. A covalent bond to bromine is cleaved and the displaced atom is not scattered throughout the crystal but can most likely be assigned as a bromide to an additional difference electron density peak observed in the structure. The bromide relocates to an adjacent unoccupied site where promising interactions to protein residues stabilize its position. These findings were verified by a second similar structure determined with considerably higher radiation dose (PDB code 3onb).

© 2011 International Union of Crystallography  
Printed in Singapore – all rights reserved

**Keywords:** radiation damage; bromine cleavage; experimental phasing; aldose reductase; enzyme–inhibitor complex; protein–ligand interaction.

## 1. Introduction

Crystal structure determination of protein–ligand complexes using synchrotron radiation is one of the key steps in rational drug design. In particular, high-resolution protein structures reveal intricate details about ligand binding that can be utilized for the initial design of lead structures and their further optimization. Even small geometrical changes in a protein–ligand complex are of high interest to elucidate the free-energy contribution of certain substituents added to a promising scaffold. Additionally, high-resolution X-ray structures provide the structural basis for development, improvement and validation of predictive computational methods. Therefore, precise analysis of the relevance and reliability of such data is of utmost importance.

As a consequence of the continuous improvement of experimental methods, particularly by the use of synchrotron radiation combined with cryoprotective techniques, the atomic resolution of protein–inhibitor complexes becomes feasible (Dauter *et al.*, 2010). Even by applying standard protocols, non-expert users can obtain such high-resolution data. However, the danger of false interpretation exists especially owing to limited experience considering the enormous amount of detail contained in these high-resolution structures.

The impact of highly intense X-ray radiation on macromolecules during diffraction experiments is widely known and hardly avoidable (Borek *et al.*, 2007; Nave & Garman, 2005; Murray *et al.*, 2005). Radiation damage manifests in crystal disorder and increasing mosaicity as well as specific chemical

modifications observed for certain residues (Garman, 2010; Ravelli & Garman, 2006). In particular, covalent bond breakage involving anomalous scatterers occurs repeatedly and causes problems when performing single-wavelength anomalous dispersion/multiple-wavelength anomalous dispersion (SAD/MAD) experiments including data collected close to the absorption edge of a specific atom type (Peterson *et al.*, 1996; Ennifar *et al.*, 2002; Schiltz *et al.*, 2004). Usually the cleavage product gains much residual mobility and distributes across the entire crystal. Thus, hardly any contribution to the diffraction pattern can be detected. In other cases the particle cleaved off assembles systematically at one spot to produce a novel peak in the difference electron density map. Such peaks have to be interpreted with care, as they easily arise to a level falsely suggesting the presence of an additional water molecule next to the cleavage site.

In a series of high-resolution X-ray structures of human aldose reductase (hAR) mutants complexed with brominated inhibitors (Koch *et al.*, 2010), an additional difference electron density peak near the inhibitor could falsely be interpreted as additionally incorporated water owing to short distances to the inhibitor molecule. Nevertheless, the occurrence of this peak in several X-ray structures of the series demanded detailed investigation.

In this study we provide evidence that selective radiation damage on a hAR mutant crystal occurs. A highly potent and fully occupied inhibitor is debrominated although the experiment was performed with moderate radiation dose. The overall binding mode is not affected and the inhibitor does not

relocate. Furthermore, the special environment in the binding pocket prevents the liberated bromine from deserting but holds it in an adjacent position. This position could be assigned to the unallocated density peak present in several high-resolution structures of this protein determined with two brominated structurally similar inhibitors.

## 2. Experimental methods

### 2.1. hAR crystals

Mutation, expression and crystallization of hAR followed known protocols (Steuber *et al.*, 2008). *Via* site-directed mutagenesis, Thr 113 was replaced by alanine. hAR was expressed in *Escherichia coli* and prepared in pH 5 Tris buffer. The protein was equilibrated with NADP<sup>+</sup> and IDD594 (final protein/cofactor/inhibitor ratio 1/2/2) at 277 K *via* the hanging-drop vapor diffusion method. Crystals grew overnight after microseeding at 291 K. Cryofreezing was carried out using a cryoprotecting solution containing 40% PEG 6000 in liquid nitrogen.

### 2.2. Data collection and processing

Data for set A were collected of one IDD594–hAR-complex crystal at 100 K. 600 images were collected at a wavelength of 0.91841 Å (13.4998 keV) without interruption to ensure a moderate state of radiation damage. The detector (CCD, Rayonix MX-225) was at a distance of 90 mm from the crystal. The data were split into three subsets of 200 images each (subsets 1, 2, 3). For each subset separately and for the complete dataset all reflections were processed and scaled both for native and anomalous scattering using the *HKL2000* package (Otwinowski & Minor, 1997). For subsets 1–3, scaling and merging statistics are displayed in Table 1(b). Additionally, a second crystal of the same complex was used for collection of 180 images at 100 K at 0.9100 Å (13.6246 keV; set B). The detector (MARMOSAIC 225 MM CCD) was at a distance of 160 mm from the crystal. Processing and scaling was performed as for the first crystal, using the entire dataset of 180 images.

### 2.3. Phasing, structure determination and refinement

Structure factor data for both SAD experiments were prepared using *SHELXC*. A substructure search for one Br atom, based on intensity differences, was performed with *SHELXD* using the implemented dual-space recycling algorithm (Sheldrick *et al.*, 2001). The program was used as implemented in the *HKL2MAP* interface using data for 20–1.6 Å and 100 trials (Sheldrick, 2008, 2010; Schneider & Sheldrick, 2002; Pape & Schneider, 2004). Phases were improved by density modification using the sphere-of-influence method as implemented in *SHELXE* (Sheldrick, 2002, 2010). Both native data and *SHELXE* output phases were merged and used for model building starting with the obtained polyaniline chain of the *SHELXE* run for set A. For set B, obtained peak positions from *SHELXD* were used for initial phasing in *SHELXE*. The determined bromine sites found in

**Table 1**

(a) Data processing and refinement statistics.

Values shown in parentheses are for the outermost shell.

	Set A	Set B
PDB entry	3onc	3onb
Data collection and processing		
No. of crystals used	1	1
Wavelength (Å)	0.91841	0.9100
Space group	<i>P</i> 2 <sub>1</sub>	<i>P</i> 2 <sub>1</sub>
Unit-cell parameters		
<i>a</i> , <i>b</i> , <i>c</i> (Å)	49.3, 66.8, 47.3	49.1, 66.5, 47.1
$\beta$ (°)	92.4	92.4
Matthews coefficient (Å <sup>3</sup> Da <sup>-1</sup> )	2.1	2.1
Solvent content (%)	40.4	40.6
Diffraction data		
Resolution range (Å)	20–1.06 (1.08–1.06)	30–1.45 (1.48–1.45)
Unique reflections	133027 (6568)	48763 (1928)
<i>R</i> ( <i>I</i> )sym (%)	4.8 (9.8)	3.9 (15.3)
Completeness (%)	96.5 (96.1)	90.6 (71.8)
Redundancy	6.1 (6.0)	3.5 (2.7)
<i>I</i> / $\sigma$ ( <i>I</i> )	30.6 (20.3)	30.0 (7.5)
Refinement		
Resolution range (Å)	10–1.06	10–1.45
Reflections used in refinement (work/free)	126315/6654	46219/2439
<i>R</i> <sub>final</sub> all reflections (work/free) (%)	9.6/11.8	11.7/17.6
<i>R</i> <sub>final</sub> reflections with <i>F</i> > 4 $\sigma$ <i>F</i> (work/free) (%)	9.5/11.5	11.3/16.9
Protein residues	313	312
Inhibitor atoms	24	24
Water molecules	462	372
RMSDs		
Bonds (Å)	0.013	0.008
Angles (°)	2.0	1.9
Ramachandran plot: residues in		
most favored regions (%)	90.5	91.2
additionally allowed regions (%)	9.5	8.8
generously allowed regions (%)	0.0	0.0
Mean <i>B</i> -factor (Å <sup>2</sup> )		
Protein	7.3	16.1
Inhibitor	5.0	14.4
Water molecules	20.2	29.1

(b) Data processing and refinement statistics for subsets 1–3.

	Subset 1	Subset 2	Subset 3
Diffraction data			
Resolution range (Å)	20–1.06 (1.08–1.06)		
<i>R</i> ( <i>I</i> )sym (%)	4.4 (8.1)	3.8 (7.2)	4.3 (8.4)
Completeness (%)	83.4 (87.8)	83.5 (88.8)	83.4 (87.5)
Redundancy	2.4 (2.2)	2.4 (2.2)	2.4 (2.2)
<i>I</i> / $\sigma$ ( <i>I</i> )	18.4 (11.4)	19.6 (12.5)	19.0 (11.7)

the anomalous maps generated from the *SHELXE* phases were not sufficient to enable a polyaniline tracing of the molecule as done for set A. Nevertheless, the peak heights after 20 cycles of phase improvement in *SHELXE* are listed in Table 3.

For both datasets, structure determination was carried out additionally *via* molecular replacement and rigid-body refinement using a hAR reference structure (PDB code 1e13; Calderone *et al.*, 2000) in *CNS* (Brünger *et al.*, 1998). The

**Table 2**

Experimental set-up and estimated dose values.

	Number of frames	Exposure time per frame (s)	Oscillation width (°)	Total time of exposure (s)	Estimated flux (photons s <sup>-1</sup> )	Dose per set (MGy)
Set A	600	2	0.5	1200	$1.90 \times 10^{11}$	3.96
Subset 1	200	2	0.5	400	$1.90 \times 10^{11}$	1.32
Subset 2	200	2	0.5	400	$1.90 \times 10^{11}$	1.32
Subset 3	200	2	0.5	400	$1.90 \times 10^{11}$	1.32
Set B	180	1.7	1.0	306	$1.79 \times 10^{11}$	17.7

following refinement was computed using *SHELXL* (Sheldrick & Schneider, 1997). Model building was performed using *Coot* (Emsley & Cowtan, 2004). The refined parameters include atomic coordinates, atomic occupancy and anisotropic displacement parameters. Refinement statistics are presented in Table 1(a).

#### 2.4. Dose rate calculations

The dose for each dataset and the subsets was calculated using *RADDOSE* (Paithankar *et al.*, 2009; Murray *et al.*, 2004) based on the electron flux estimated from the data collection reported in Table 2. The flux density was calculated according to the beam size and flux reported on the corresponding synchrotron source website and determined as  $1.1 \times 10^7$  photons mm<sup>-2</sup> s<sup>-1</sup> for set A and  $2.1 \times 10^8$  photons mm<sup>-2</sup> s<sup>-1</sup> for set B. Crystal sizes were determined as approximately  $0.13 \times 0.06 \times 0.01$  mm for both crystals. The beam size was  $0.19 \times 0.09$  mm for set A and  $0.09 \times 0.01$  mm for set B.

#### 2.5. CSD searches

Cambridge Structural Database (CSD, version 5.31; Allen, 2002) searches were carried out using *ConQuest* (version 1.2). A backbone peptide without side-chain information was defined [smiles string CNC(C)=O] and the contact of an unbound bromide to the nitrogen was determined as the distance to be investigated. 160 total contacts were observed in 73 hits. In a second search a contact of bromide to a CH<sub>2</sub> group without further restraints [smiles string CC([H]H)C] was chosen. Here, 833 hits resulted in 1979 total observations.

### 3. Results

#### 3.1. Strategy

To confirm the hypothesis of a debrominated inhibitor and verify the reproducibility of the additional positive difference electron density peak observed in another study with a series of hAR mutant complexes (Koch *et al.*, 2010), a hAR T113A mutant in complex with IDD594 was structurally determined. One crystal of this complex was exposed to an enhanced synchrotron radiation dose by collecting 600 images at a wavelength of 0.91841 Å to ensure a moderate amount of radiation damage. Data (set A, PDB code 3onc) of this crystal were searched for anomalous scatterers to explore the position and occupancy of the heavy-atom substituent of the ligand. Therefore, a Br-substructure determination based on intensity differences using the dual-space recycling algorithm

implemented in *SHELXD* was performed (Sheldrick *et al.*, 2001; Sheldrick, 2010). For deeper insights into the successive cleavage of the bromine-substituted phenyl moiety the dataset was split into three parts, where the first part (subset 1) contained the first 200 images collected at the beginning of the experiment with supposedly the least radiation damage of the sample. The second and third part (subsets 2 and 3) each consisted of 200 of the subsequently collected images (see Table 2).

Furthermore, another crystal of the same mutant protein inhibitor complex was used to collect a second dataset (set B, PDB code 3onb). To ensure debromination to a considerably high amount the crystal was exposed to an extensively higher radiation dose at  $\lambda = 0.9100$  Å. The collected image number and the estimated radiation dose for both datasets and the three subsets of set A are displayed in Table 2.

To confirm the hypothesis of a dose dependency of the cleavage, a third crystal of the alanine-IDD594 complex was collected in-house at a wavelength of 1.54178 Å.

#### 3.2. Radiation-induced bromine cleavage

The structure determination of the hAR T113A mutant complexed with IDD594 was accomplished by molecular replacement and subsequent refinement to 1.06 Å resolution. The structure results in an accurate model with good refinement statistics (set A, Table 1). The electron density of protein and ligand atoms is well defined. The high resolution reveals a number of details in the active-site region that are in good agreement with an atomic-resolution structure of this inhibitor complexed to the wild-type protein (PDB code 1us0; Howard *et al.*, 2004).

hAR is a 36 kDa protein of 315 amino acids folded into a TIM barrel. The active site is located near the C-terminus and is able to exhibit an additional interaction site to accommodate substrates of varying shape. A C-terminal loop containing Leu 300 provides the required adaptivity of the protein to form this specificity pocket (El-Kabbani *et al.*, 2004; Singh *et al.*, 2006).

The inhibitor IDD594 interacts with the anionic site of the binding pocket *via* its carboxylate-type anchor group (Fig. 1). A  $\pi$ -stacking of the central fluorine-substituted phenyl moiety with Phe 122 forms another key interaction. Leu 300 is known to perform large conformational changes upon ligand binding; it flips and thus opens the above-mentioned specificity pocket which enables the ligand to interact with Trp 111 *via* stacking between this amino acid and the terminal aromatic moiety of the ligand. In the rear pocket the bromine substituent interacts

with the mutated residue Ala 113. A detailed analysis of the differences in binding mode between wild-type and mutant complex is reported elsewhere (Koch *et al.*, 2010). Upon collection of the first dataset of the alanine mutant IDD594 complex (PDB code 3lql), bromine cleavage became conspicuous in the first place. The sample was exposed to a dose of 11 kGy. In the present study the radiation dose was considerably higher, though, at 4.0 MGy, still in a moderate range (see Table 2). This corresponds to a little more than half the dose of 6.4 MGy applied in a similar study on a complex of hAR with IDD594 where considerable damage of the protein was observed (Petrova *et al.*, 2009; PDB code 3ghu). A comparison of the latter wild-type complex and our alanine mutant complex shows no radiation-induced damage of protein residues in set A. Even residues which are likely to be decarboxylated upon intense radiation remain unaffected. Still, the absorbed dose of the crystal in set A is far below the suggested upper radiation dose limit for protein crystals during data collection of 30 MGy (Owen *et al.*, 2006). The occurrence of debromination of the inhibitor IDD594 was initially suggested by close inspection of the difference Fourier maps calculated during *SHELXL* refinement. The  $2F_o - F_c$  map showed high peak intensities and well defined density for protein, cofactor and inhibitor. Nevertheless, the  $F_o - F_c$  difference density map revealed an additional peak at a distance of about 2.1 Å while reduced occupancy is suggested at the expected atomic center of the covalently attached Br atom by negative difference electron density (Fig. 1). In consequence, the occupancy of the Br atom was refined while the rest of the inhibitor atoms were kept at full occupancy, resulting in a final bromine occupancy of 72.8% (see Table 3).

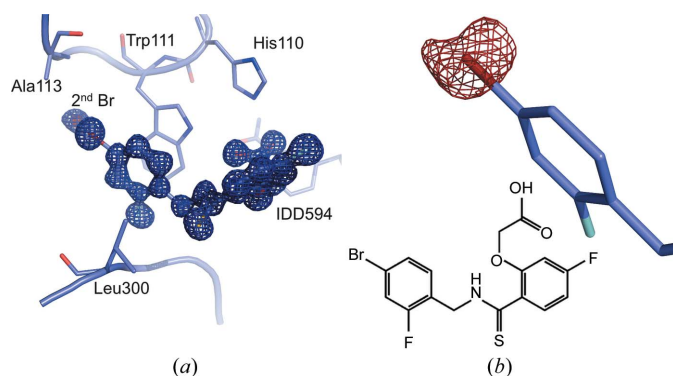


**Figure 1**  
(a) Position of IDD594 in the binding pocket of hAR. The  $2F_o - F_c$  electron density of the inhibitor is displayed at  $2\sigma$  in blue. (b) Difference density around the bromine substituent of IDD594, showing a negative peak at the center of the Br atom (red). This indicated incomplete occupancy and was the starting point for further investigations. The  $F_o - F_c$  difference electron density is displayed at  $2\sigma$ .

**Table 3**

Anomalous peak heights after *SHELXE* phasing and occupancy decrease of bromine sites from final structural refinement.

For sets A and B and the three subsets the found anomalous peaks are given with their fractional coordinates  $x, y, z$ . The peak heights ( $h$ ) observed in the anomalous map are given in  $\sigma$ . In the next column the interatomic distances to the first peak are given. In the last two columns the refined occupancies of the first and second bromine position are listed.

	Images	$x$	$y$	$z$	$h$	Distance (Å)	Refined 1st Br occupancy (%)	Refined 2nd Br occupancy (%)
Set A	1–600	0.3033	0.9998	0.1949	168.3		72.8	27.2
		0.3108	0.9676	0.2030	29.2	2.22		
Subset 1	1–200	0.1966	0.2971	0.3052	122.7		69.6	30.4
		0.2366	0.2850	0.3426	8.5	2.71		
Subset 2	201–400	0.3029	0.7187	0.1948	104.7		62.7	37.3
		0.3089	0.6852	0.2026	23.9	2.29		
Subset 3	401–600	0.8035	0.4139	0.1954	103.7		61.7	38.3
		0.8109	0.3805	0.2034	29.4	2.29		
Set B	1–180	0.8043	0.6959	0.1971	76.1		52.0	48.0
		0.8162	0.7307	0.2002	17.4	2.38		
		0.8183	0.6589	0.1995	12.4	2.56		

An additional dataset of the same alanine mutant complex with IDD594 collected at our in-house radiation source shows the covalently bound bromine in full occupancy, the same as the residual inhibitor atoms and binding site residues. This strongly suggests a dose dependency of the cleavage of the carbon–bromine bond.

To investigate the decrease of the bromine signal as a consequence of radiation damage, the complete set A was searched for anomalous scatterers by bromine substructure determination based on anomalous intensity differences as implemented in *SHELXC,D,E* (Sheldrick, 2010). One bromine site corresponding to the atomic position of the covalently attached bromine at the terminal phenyl ring could be determined using *SHELXD* for the complete dataset and for each subset using anomalous data in the 20–1.6 Å resolution range. Upon heavy-atom site search by *SHELXD*, the program by default sets the strongest anomalous signal as the first heavy-atom site to an occupancy of 1. Subsequently found signals are calculated with relative occupancy according to the initial assignment. Thus, when searching for one anomalous scatterer in the dataset, a straight drop in occupancy to values below approximately 30% for a second site is desired.

The bromine site occupancies in the dataset indicate a strong anomalous signal dropping to values below 30% occupancy for a second bromine site (see Fig. 2, black squares). The positions of the first bromine sites show up to be identical for the different solutions obtained for the different subsets. It coincides with the ligand's bromine position indicated in the initial electron density map obtained by *SHELXE* (see Fig. 3a). In this first model, not only the protein main chain is clearly defined, and the architecture of the polyaniline solution fits well into the density. Additionally, each ligand atom can be clearly identified. However, while the drop in occupancy of the bromine sites is even more pronounced when only regarding the *SHELXD* result of the first 200 images of subset 1, the differentiation becomes less distinctive once images of subsets 2 and 3 collected after absorbance of a considerably higher radiation dose are used for heavy-atom

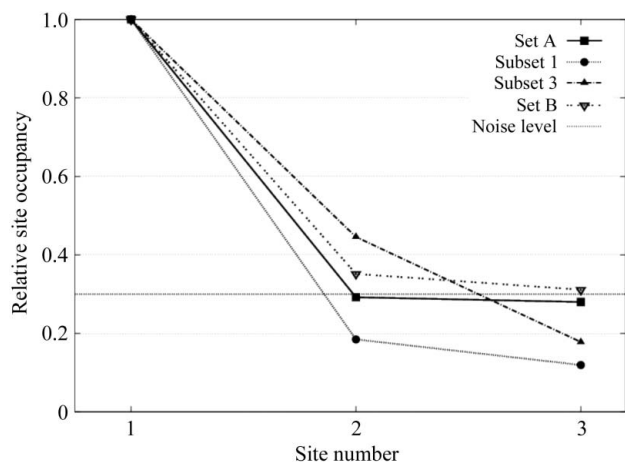


**Figure 2** Bromine site occupancy *versus* peak number (as calculated by *SHELXD*) for the different datasets. The strongest anomalous signal is set to 1 by default; subsequently found atoms are calculated with relative occupancy. The clear drop in the occupancy in set A (squares) indicates a high discrimination of the determined bromine site in contrast to the noise signal. The drop even increases when only subset 1 is used for the calculation (circles). The second anomalous signal in subset 3 (filled triangles) is still significantly higher than noise. In set B (upturned triangles), exposed to a significantly higher radiation dose, a search for one bromine site immediately resulted in one bromine site and two potential minor sites.

location with *SHELXD* (Table 2 and Fig. 2). In the subset considering images at the end of the experiment, the occupancy of a potential second and third bromine site is increased compared with the beginning of the data collection. It still denotes the presence of a Br atom at the first site but suggests a decreasing signal. In the electron density the peak of diffracting electrons at this first bromine position gradually declines with increasing image number. This correlates well

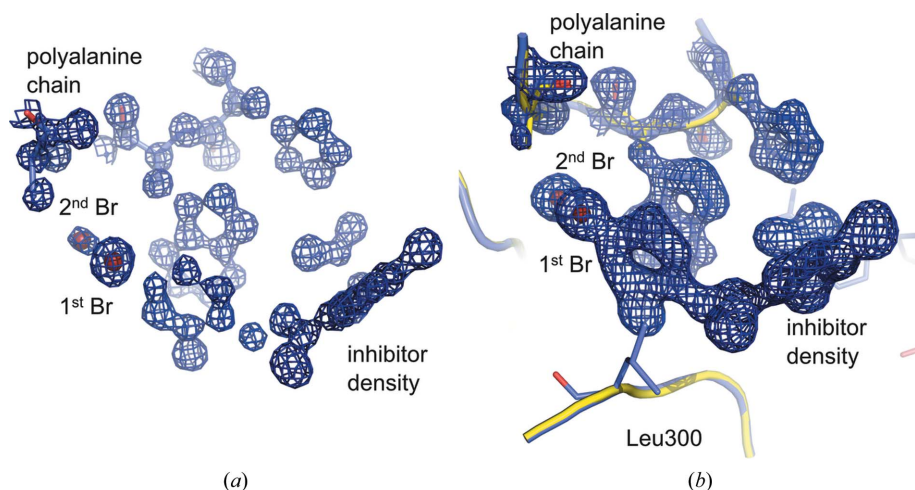


**Figure 3** Two Br atoms (red) were found in the SAD experiment for set A (a) and set B (b). Each protein and ligand atom can be identified in the electron density. The first bromine site matches the covalently attached bromine position in the inhibitor-shaped density. The second bromine site agrees with an adjacent density peak. (a) The initial polyaniline chain (blue) with the corresponding  $2F_0 - F_c$  map of the *SHELXE* run is displayed. (b) The initial polyaniline chain (yellow) superimposed with the refined final protein residues (blue) of set B. The initial  $2F_0 - F_c$  map as a result of the *SHELXE* run is displayed at  $1.5\sigma$ .

with a decrease of anomalous scattering power at this position and suggests progressive cleavage of the bromine substituent from the inhibitor.

These findings are further supported by the intensities of the determined bromine sites found in the anomalous maps generated from the final *SHELXE* phases. While for the complete set A two peaks ( $168.3\sigma$  and  $29.2\sigma$ ) were observed at an interatomic distance of  $2.22 \text{ \AA}$ , for subset 1 only a single peak was observed in the anomalous map at  $122.7\sigma$  (Table 3). In subset 2 the main site shows up at  $104.7\sigma$  and the minor site at  $23.9\sigma$ . In subset 3 the main site has almost the same peak height ( $103.7\sigma$ ), but the minor site is slightly increased to  $29.4\sigma$ . In all cases the second minor site is about  $2.2 \text{ \AA}$  apart from the main site, which is also observed for the fully refined structures.

The disruption of the Br atom off the aromatic moiety increases its residual mobility and thus enables the Br atom to relocate. This cleavage product is most likely to be a bromide ion (Oliéric *et al.*, 2007).

### 3.3. Second bromine site indicates additional interaction site

Unexpectedly, the loss of the halogen scattering power at the first site particularly experienced in the last subset 3 is accompanied by the appearance of a second anomalous signal with lower occupancy. Still, the signal is clearly discriminated from noise by a further clear drop to a third bromine site which falls beyond the noise level (see Fig. 2, filled triangles) and thus denotes the presence of a second heavy-atom site. This position is occupied by bromine arising as a cleavage product of the inhibitor. Remarkably, the coordinates of this second peak refine to a position adjacent to the first bromine site found by *SHELXD* analysis. In the corresponding electron density map, this second position matches a location

in between the inhibitor's original bromine substituent and the backbone nitrogen of Ala 113 of the protein. At this position an additional positive difference density peak appears when the structure is determined by molecular replacement with a model considering the protein atoms only.

We attempted to confirm the position of this additional peak by collecting diffraction data of another crystal of the same complex. It was exposed to a considerably higher dose of  $17.7 \text{ MGy}$  (set B, see Table 2) and consistently showed the position of the cleavage product.

Again, both structure solution *via* molecular replacement and *via* bromine substructure determination were applied to the entire dataset B. The overall protein structure and conformation of pocket residues match well with the wild-type model and the results

obtained for set A. No major changes in binding mode or ligand positions could be determined.

In the initial electron density calculated by only assigning the protein atoms and neglecting ligand and cofactor, the atoms occupying the binding pocket are clearly visible in the difference electron density. Each ligand atom is easily identified, and additional density adjacent to the Br atom with equal peak height suggests the presence of the second bromine site.

Consequently, the model for further refinement included two Br atoms: one covalently bound to the ligand, the other a single unbound bromine. Their occupancies were refined independently in the first place which resulted in a 47:45 ratio. This indicates an almost equal population for both sites and an overall negligible loss of a bromide to additional positions. The occupancy of the liberated anion is remarkably high and almost equal to the ligand-bound atom. In later refinement cycles the occupancy of both atoms was refined dependently neglecting any loss of bromine. This resulted in a final occupancy of 52% for the bromine covalently bound to the ligand and 48% for the bromide ion (Table 3).

As for set A, a heavy-atom search of set B was performed. The search for one heavy-atom site displayed one bromine site and two potential minor sites (see Fig. 2, upturned triangle). Similarly to the first dataset, the positions of the heavy atoms are visible as separate and adjacent density peaks in the first electron density maps (see Fig. 3*b*). The peak heights after 20 cycles of phase improvement in *SHELXE* are listed in Table 3.

Unexpectedly, the bromide does not disappear and scatter throughout the entire crystal owing to high mobility, but accommodates to a distinct position with almost the converse occupancy to the original site from where the bromine has been released owing to radiation damage. It is within 2.1 Å of its original ligand-bound position. However, the distance to neighboring amino acids is larger. The Ala 113 methyl group is at a distance of 3.1 Å while the ring atom C  $\delta$  of Pro 310 and the bridging C  $\beta$  of Trp 111 are at 3.4 Å and 3.7 Å, respectively. The backbone nitrogen of Ala 113 most likely donates its hydrogen to a hydrogen bond with the bromide with a distance of 3.5 Å (Fig. 4). Reported distances of bromide ions contacting N atoms fall between 3.1 and 3.8 Å, while contacts to hydrophobic C atoms are found in the range 3.5–4.1 Å (see Fig. 5), as a detailed analysis of highly resolved small molecule crystal structures in the CSD shows. The determined interaction distances in the complex satisfy these expectations.

#### 4. Discussion

The radiation-induced cleavage of a bromide ion from a halogenated inhibitor during X-ray structure determination has been reported previously (Petrova *et al.*, 2009; Garman & Nave, 2009). The bond between a bromine

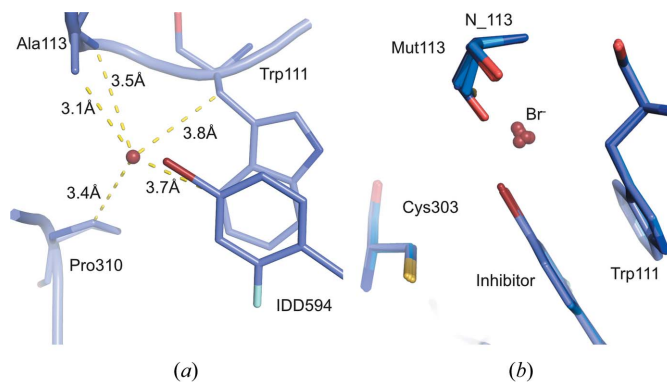


**Figure 4**

(*a*) The distance of the isolated bromide ion to surrounding atoms is displayed. The amide nitrogen of Ala 113 presents its hydrogen towards the ion. All determined distances to the nearest atoms lay within 3.0–3.8 Å and fit into reported data from the CSD. (*b*) Superposition of T 113 Ala, Cys, Ser mutant structures of hAR complexed IDD 594 and IDD 388. All determined bromide ions occupy the same position.

substituent and a phenyl moiety is likely to break owing to strong absorbance of radiation and subsequent changes in the electron configuration of bromine. This will depend on the dose absorbed during the experiment and occurred not only for extensive dose absorption in the second experiment with a long exposure time. It is also consistent with a study of the same inhibitor in a high-resolution wild-type complex of hAR with IDD 594 recorded at  $\lambda = 0.66$  Å (PDB code 1us0) where the final bromine occupancy is refined with a minor loss still showing 94% occupancy (Howard *et al.*, 2004). In contrast to this, an in-house-collected dataset ( $\lambda = 1.54$  Å) shows IDD 594 intact without loss of bromine.

In addition to the absolute dose absorbed during an experiment, the wavelength used in the diffraction experiment should be taken into account (Leiros *et al.*, 2006). The Br *K*-edge is found at 0.9204 Å which falls close to standard wavelengths used at synchrotron sources. Set A was collected at 0.91841 Å (BESSY), and set B at 0.9100 Å (Swiss Light Source) which most likely enhances the cleavage probability

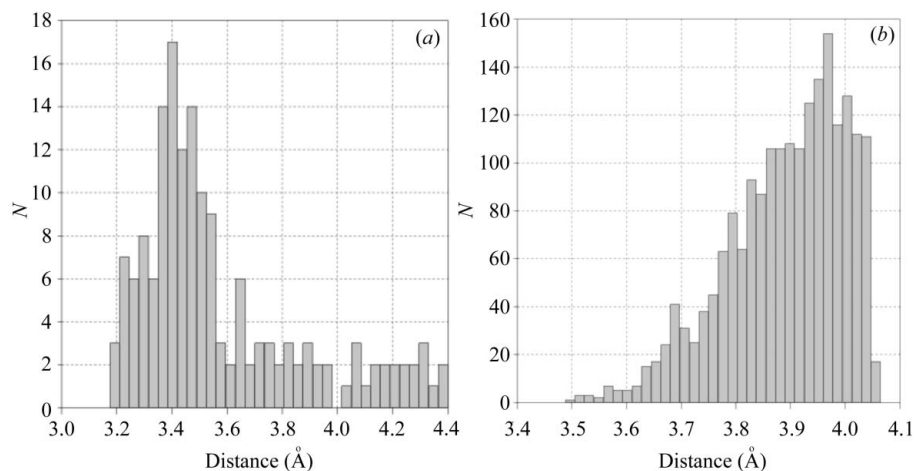


**Figure 5**

Histograms of observed bromide contact distances in the CSD. (*a*) Contact counts of bromide to amide N atoms are displayed dependent on the interaction distance in Å. (*b*) Contacts to secondary C atoms are displayed.

in both experiments. In contrast, 1us0 was collected at 0.653 Å and shows a remarkably higher bromine occupancy of 94% as mentioned above. Presumably the small deviation of the collection wavelength from the Br *K*-edge also explains the relatively high cleavage rate of 30% in set A and in set B (50%) where a fivefold-higher radiation dose was used. While *de novo* phasing of aldose reductase is not required since there are many excellent high-resolution structures available for molecular replacement, exploitation of the anomalous signal for bromine substructure determination proved to be a valuable tool to unambiguously characterize the additional density peak as bromine.

The close spatial rearrangement of the cleaved bromide ion to a distinct adjacent position appears remarkable. This position became evident in both diffraction experiments evaluated in this study. Interestingly, a matching position for such a bromide ion could be detected in a series of protein–ligand complexes determined with other mutants of the same protein. The disruption of the covalent carbon–bromine bond at the phenyl moiety was observed in these mutant complexes with IDD594 and a similar ligand, IDD388 (*e.g.* T113S/T113C complexed with IDD594, PDB code 3ld5, 3lbo; see Fig. 4*b*). Furthermore, even in the high-resolution wild-type complex (PDB code 1us0), a positive density in the  $F_o - F_c$  difference density map appears at  $0.35 \text{ e} \text{ \AA}^{-3}$  at the same position.

The consistency of this position suggests the availability of unoccupied space accessible to form new interactions with the enzyme. In the T113A mutant complex with IDD594 this site remains unoccupied in the first place.

A free volume of approximately  $18 \text{ \AA}^3$  can be assigned to this location (see Fig. 6). Obviously this vacancy is too small to trap a single water molecule. Most likely the released bromide ion is captured by a hydrogen bond with Ala 113 while further hydrophobic interactions are experienced mainly with C atoms of surrounding amino acids. Depending on the degree of its polarization, the obtained distances build a favorable interaction pattern for the highly polarizable bromide ion.

In other complexes of both wild-type and mutated protein of hAR formed with the non-brominated zopolrestat, a fluorine atom, being part of a trifluoromethyl moiety, partly

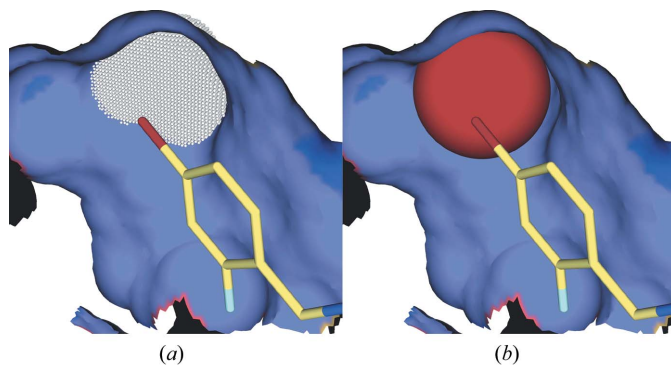


**Figure 6**  
(*a*) An additional free volume near Ala 113 of about  $18 \text{ \AA}^3$  indicated by the white dots cannot be occupied by the inhibitor. (*b*) The cleaved bromide ion is represented as a sphere the size of its van der Waals radius. The additional volume is almost completely filled by the bromide.

occupies this gap. However, owing to the geometry of this substituent and the much smaller van der Waals radius of fluorine, it cannot fully occupy the space. As a consequence, the distance between the fluorine atom and N–H of Ala 113 expands to  $4.4 \text{ \AA}$ , which can at most be described as a weak van der Waals interaction.

In the complexes of the wild-type protein as well as the mutant complexes with IDD594, this volume can partly be occupied by the threonine, cysteine or serine residue 113. Nevertheless, whichever conformer of this residue is formed, a certain volume remains unallocated. Though the affinity of the inhibitor to the protein is high, the inhibitor's substituents cannot provide a perfect shape complementarity between protein and ligand functional groups. However, incorporation of an additional water molecule into this remaining space seems to be energetically unfavorable, most likely owing to entropic costs. Presumably this would not outweigh a possible increase of protein–inhibitor interactions.

We thank Alberto Podjarny for providing the inhibitors and seeds; the Cambridge Crystallographic Data Centre (Cambridge, UK) for providing a copy of the Cambridge Structural Database, and Elspeth Garman (University of Oxford, UK) for a copy of *RADDOSE*. We kindly acknowledge the beamline support staff of BESSY (Berlin, Germany) and Swiss Light Source for their advice during data collection, as well as both synchrotrons for financial support of travel costs. This work was funded by Deutsche Forschungsgesellschaft under contract KL1204/3-5. We thank Gerd Neudert for help with the CSD and volume calculations.

## References

- Allen, F. H. (2002). *Acta Cryst.* **B58**, 380–388.  
 Borek, D., Ginell, S. L., Cymborowski, M., Minor, W. & Otwinowski, Z. (2007). *J. Synchrotron Rad.* **14**, 24–33.  
 Brünger, A. T., Adams, P. D., Clore, G. M., DeLano, W. L., Gros, P., Grosse-Kunstleve, R. W., Jiang, J.-S., Kuszewski, J., Nilges, M., Pannu, N. S., Read, R. J., Rice, L. M., Simonson, T. & Warren, G. L. (1998). *Acta Cryst.* **D54**, 905–921.  
 Calderone, V., Chevrier, B., Van Zandt, M., Lamour, V., Howard, E., Poterszman, A., Barth, P., Mitschler, A., Lu, J., Dvornik, D. M., Klebe, G., Kraemer, O., Moorman, A. R., Moras, D. & Podjarny, A. (2000). *Acta Cryst.* **D56**, 536–540.  
 Dauter, Z., Jaskolski, M. & Wlodawer, A. (2010). *J. Synchrotron Rad.* **17**, 433–444.  
 El-Kabbani, O., Ruiz, F., Darmanin, C. & Chung, R. P. (2004). *Cell. Mol. Life Sci.* **61**, 750–762.  
 Emsley, P. & Cowtan, K. (2004). *Acta Cryst.* **D60**, 2126–2132.  
 Ennifar, E., Carpentier, P., Ferrer, J.-L., Walter, P. & Dumas, P. (2002). *Acta Cryst.* **D58**, 1262–1268.  
 Garman, E. F. (2010). *Acta Cryst.* **D66**, 339–351.  
 Garman, E. F. & Nave, C. (2009). *J. Synchrotron Rad.* **16**, 129–132.  
 Howard, E., Sanishvili, R., Cachau, R., Mitschler, A., Chevrier, B., Barth, P., Lamour, V., Van Zandt, M., Sibley, E., Bon, C., Moras, D., Schneider, T., Joachimiak, A. & Podjarny, A. (2004). *Proteins Struct. Funct. Bioinf.* **55**, 792–804.  
 Koch, C., Heine, A. & Klebe, G. (2010). *J. Mol. Biol.* **406**, 700–712.  
 Leiros, H., Timmins, J., Ravelli, R. & McSweeney, S. (2006). *Act. Cryst. D*, **62**, 125–132.

- Murray, J. W., Garman, E. F. & Ravelli, R. B. G. (2004). *J. Appl. Cryst.* **37**, 513–522.
- Murray, J. W., Rudiño-Piñera, E., Owen, R. L., Grininger, M., Ravelli, R. B. G. & Garman, E. F. (2005). *J. Synchrotron Rad.* **12**, 268–275.
- Nave, C. & Garman, E. F. (2005). *J. Synchrotron Rad.* **12**, 257–260.
- Oliéric, V., Ennifar, E., Meents, A., Fleurant, M., Besnard, C., Pattison, P., Schiltz, M., Schulze-Briese, C. & Dumas, P. (2007). *Acta Cryst.* **D63**, 759–768.
- Otwinowski, Z. & Minor, W. (1997). *Methods Enzymol.* **276**, 307–326.
- Owen, R. L., Rudiño-Piñera, E. & Garman, E. F. (2006). *Proc. Natl Acad. Sci. USA*, **103**, 4912–4917.
- Paithankar, K. S., Owen, R. L. & Garman, E. F. (2009). *J. Synchrotron Rad.* **16**, 152–162.
- Pape, T. & Schneider, T. R. (2004). *J. Appl. Cryst.* **37**, 843–844.
- Peterson, M. R., Harrop, S. J., McSweeney, S. M., Leonard, G. A., Thompson, A. W., Hunter, W. N. & Helliwell, J. R. (1996). *J. Synchrotron Rad.* **3**, 24–34.
- Petrova, T., Lunin, V. Y., Ginell, S., Hazemann, I., Lazarski, K., Mitschler, A., Podjarny, A. & Joachimiak, A. (2009). *J. Mol. Biol.* **387**, 1092–1105.
- Ravelli, R. B. & Garman, E. F. (2006). *Curr. Opin. Struct. Biol.* **16**, 624–629.
- Schiltz, M., Dumas, P., Ennifar, E., Flensburg, C., Paciorek, W., Vonnrhein, C. & Bricogne, G. (2004). *Acta Cryst.* **D60**, 1024–1031.
- Schneider, T. R. & Sheldrick, G. M. (2002). *Acta Cryst.* **D58**, 1772–1779.
- Sheldrick, G. M. (2002). *Z. Kristallogr.* **217**, 644–650.
- Sheldrick, G. M. (2008). *Acta Cryst.* **A64**, 112–122.
- Sheldrick, G. M. (2010). *Acta Cryst.* **D66**, 479–485.
- Sheldrick, G. M., Hauptman, H. A., Weeks, C. M., Miller, M. & Usón, I. (2001). *International Tables for Crystallography*, Vol. F, edited by E. Arnold and M. Rossmann, pp. 333–351. Dordrecht: Kluwer Academic Publishers.
- Sheldrick, G. M. & Schneider, T. (1997). *Methods Enzymol.* **277**, 319–343.
- Singh, R., White, M. A., Ramana, K. V., Petrash, J. M., Watowich, S. J., Bhatnagar, A. & Srivastava, S. K. (2006). *Proteins Struct. Funct. Bioinf.* **64**, 101–110.
- Steuber, H., Heine, A., Podjarny, A. & Klebe, G. (2008). *J. Mol. Biol.* **379**, 991–1016.